npj | 2D materials and applications

www.nature.com/npj2dmaterials

ARTICLE OPEN

Electrically tunable lateral spin-valve transistor based on bilayer CrI_3

Damiano Marian[1]✉, David Soriano[1], Emmanuele Cannavó[1], Enrique G. Marin[2] and Gianluca Fiori[1]✉

The recent discovery of two-dimensional (2D) magnetic materials has opened new frontiers for the design of nanoscale spintronic devices. Among 2D nano-magnets, bilayer CrI_3 outstands for its antiferromagnetic interlayer coupling and its electrically-mediated magnetic state control. Here, leveraging on CrI_3 magnetic and electrical properties, we propose a lateral spin-valve transistor based on bilayer CrI_3, where the spin transport is fully controlled via an external electric field. The proposed proof-of-concept device, working in the ballistic regime, is able to both filter (>99%) and select ON/OFF the spin current up to a ratio of $\approx 10^2$, using a double split-gate architecture. Our results obtained exploiting a multiscale approach ranging from first-principles to out-of-equilibrium transport calculations, open unexplored paths towards the exploitation of bilayer CrI_3 or related 2D nano-magnets, as a promising platform for future electrically tunable, compact, and scalable spintronic devices.

npj 2D Materials and Applications (2023)7:42 ; https://doi.org/10.1038/s41699-023-00400-5

INTRODUCTION

The observation of long-range magnetic order in two-dimensional (2D) materials such as CrX_3 (X = Cl, Br, I) and $CrGeTe_3$[1–4] has motivated the search for new spin-based phenomena induced by magnetic-proximity effects in pure van der Waals heterostructures. These 2D nano-magnets present several advantages with respect to their three-dimensional counterparts, namely: (i) they can be easily interfaced with other 2D materials, (ii) they present stacking-dependent magnetic properties, allowing for unconventional spin configurations, and (iii) their ground state magnetization can be modified at low critical electric fields. The combination of these materials with graphene[5–7], semiconducting transition metal dichalcogenides (TMD)[8–12], or even superconducting TMDs[13], has already enabled novel van der Waals valleytronic, spintronic, and magneto-optical devices.

In this context, CrI_3 has revealed to be a particularly auspicious 2D nano-magnet, due to the observation of a stacking dependent interlayer magnetism and an unprecedented magneto-electric response. Thin CrI_3 samples show a monoclinic stacking configuration, favouring an antiferromagnetic (AFM) ground state[2,14,15]. At critical magnetic fields of around 0.6 T, the magnetic ground state in bilayer CrI_3 becomes ferromagnetic (FM). This property has led to the recent observation of giant magnetoresistance in CrI_3-based vertical magnetic tunnel junctions[16–18]. Moreover, the weak interlayer coupling in the AFM state ($\ll$1 meV) allows to switch the magnetic ground state via electrostatic doping, or by an external electric field of the order of 0.8 V/nm, under a constant magnetic bias, as recently reported for dual-gated bilayer CrI_3 field-effect devices[19–23]. These results point out the high electrical tunability of this 2D nano-magnet as compared with previous dilute magnetic semiconductors[24], opening the path towards the design of fully electrical ultrathin spintronic devices. To date, 2D nano-magnets have been mainly used as tunnel barrier in vertically-stacked magnetic tunnel junctions[16–18], in micrometer lateral magnon-based spintronic devices[25] or to induce exchange interactions in proximity to other 2D materials, e.g., graphene[26,27] and TMDs[11,13].

In this letter, we propose a 2D nano-magnet-based device architecture and operation mechanism, devising a ballistic, compact and fully electrically tunable lateral spin-valve transistor made of bilayer CrI_3. Notably, and differently from previous 2D-nano-magnet device concepts, in the proposed device: (i) there is no need of combining two or more 2D nano-magnets with different magnetic states in order to e.g., define ferromagnetic injecting source/drain contacts; as the proposed device is based uniquely on bilayer CrI_3; (ii) the transport occurs laterally (i.e., in-plane) in the 2D nano-magnet flake, in a nanometer-sized device leveraging on ballistic transport; (iii) the same material and device architecture serves both as filter and switch for the spin-carriers, simplifying the overall design and aiming at building a compact and scalable platform for spin devices and (iv) the device is fully electrically controlled, with low terminal biases, without any need of external magnetic fields.

As such, the architecture here proposed, based on bilayer CrI_3, which presents relevant technological fabrication challenges and limitations associated with the ultrascaled size of gates and spacer region, can be viewed as a testbed platform for future electrically tunable, compact, and scalable spintronic devices. In this view, this work opens the path toward the use of 2D nano-magnets within the spin-based computation paradigm[28,29]. It is worth emphasizing that the proposed device concept is not strictly related to CrI_3, but can be applied to other 2D nano-magnets such as the recently discovered $CrPS_4$[30], the high-T_C ferromagnetic semiconductors CrSBr[31–33] and CrSeBr[34], or novel ferrite ultrathin nanosheets[35].

RESULTS AND DISCUSSION

Electrical properties of bilayer CrI_3

Bilayer CrI_3 shows a monoclinic stacking (space group *c2/m*), even at low temperatures, whose origin is still far from being totally understood[36,37]. This stacking favors the interaction between t_{2g} orbitals at opposite layers, which are responsible for the weak AFM interlayer coupling observed in this material[14]. In Fig. 1a, we report the top and lateral view of the crystal lattice of bilayer CrI_3, with the

---

[1]Dipartimento di Ingegneria dell'Informazione, Università di Pisa, Via G. Caruso 16, 56122 Pisa, Italy. [2]Departamento de Electrónica y Tecnología de Computadores, Facultad de Ciencias, Universidad de Granada, Avenida de la Fuente Nueva S/N, 18071 Granada, Spain. ✉email: damiano.marian@unipi.it; gianluca.fiori@unipi.it

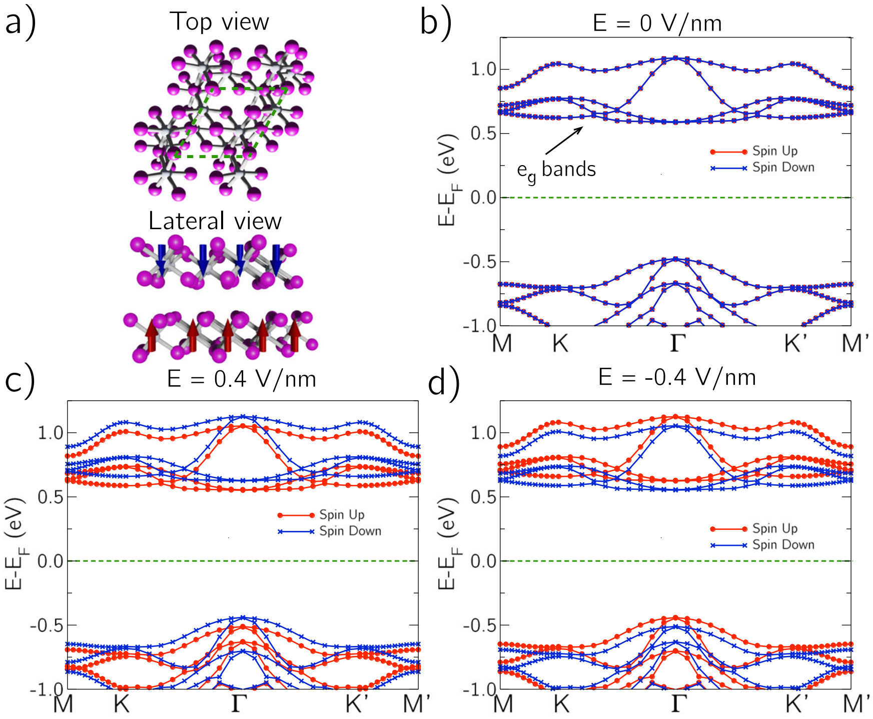

Fig. 1 Bilayer CrI$_3$ under external electric field. a Top and lateral view of the crystal structure of bilayer CrI$_3$. In the top view the elementary cell is indicated with dashed lines. In the lateral view the spin character of each layer is indicated with colored arrows (spin up in red while spin down in blue). Spin polarized band structures **b** with 0 V/nm, **c** +0.4 V/nm and **d** −0.4 V/nm electric field normal to the bilayer plane. Degenerate spin bands belong to opposite layers.

Cr atoms forming an hexagonal lattice with an edge-shared octahedral ligand field within each layer. The optimized cell lattice parameter is 6.851 Å, while the Cr-Cr interlayer distance is 6.991 Å. In Fig. 1b, we show the band structure of bilayer CrI$_3$ computed using Density Functional Theory (DFT) calculations as implemented in the Quantum Espresso ab initio suite[38] (see “Methods” for more details). The conduction bands are ~1 eV away from the valence bands, and are due to the $d_{x^2-y^2}$ and d_{z^2} orbitals of the Cr atoms, also known as the e_g manifold. In the AFM state, the spin in each layer of the bilayer stack has opposite nature, as schematically depicted in Fig. 1a, and the e_g bands of each layer are degenerated in energy, but with opposite spin (i.e., spin-up carriers in the bottom layer and spin-down carriers in the top layer).

When an external electric field of 0.4 V/nm normal to the bilayer plane is applied, electrons move between layers, breaking the spin degeneracy of the bands of 75 meV in the bottom of the conduction band (see Fig. 1c, d). Specifically, opposite electric fields produce opposite splitting of the bands: spin-up bands go down Fig. 1c or up Fig. 1d in energy depending on the electric field orientation, while the contrary happens for the spin-down bands, resulting in different energy ranges accessible for transport in the top and bottom layers. It is worth noting that the applied electric fields are below the critical electric field for the magnetic switching (~0.8 V/nm on SiO$_2$ substrate[19]), thus preserving the AFM ground state. Next, we elaborate on how the spin-electric field coupling in bilayer CrI$_3$ can be exploited for creating a device concept able to both filter spin and select ON and OFF spin-polarized currents.

Bilayer CrI$_3$ spin-valve transistor

We propose a proof-of-concept spin logic device based on bilayer CrI$_3$ that can work as a unified platform for injecting, transporting and selecting spin-charge carriers. The proposed device can be fabricated with state-of-the-art technology and consists of an oxide-encapsulated CrI$_3$ bilayer, which is electrically controlled by means of a split double-gate configuration (Fig. 2a). The first two gates (V_{g1}) act as control electrodes for the spin filtering, selecting either spin-up or spin-down carriers depending on the electric field orientation, while the second two gates (V_{g2}) turn ON and OFF the selected spin current, effectively acting as a spin detector. The proposed device works at temperature equal or below of 45 K, i.e., the Curie temperature of CrI$_3$. The overall device can produce a three-valued output, namely spin-up, spin-down, and no current. Clearly, from an experimental point of view, the only constraint is the antiferromagnetic alignment between the layers, with two possible spin configurations in the layers (not just the one shown in Fig. 1a), which give rise to opposite spin polarizations for a given sign of the gate potential. As a consequence, our device by itself is not sufficient to discern between the two different spin polarizations, which can be detected using a ferromagnetic electrode. However, it is worth mentioning that the conductivity mismatch at the interface between a highly resistive semiconductor such as CrI$_3$ and the electrode may be challenging from an experimental point of view. This issue can be solved in future devices by using with higher conductivity 2D magnets such as CrSBr or CrPS$_4$.

The working principle of the device is schematically described in Fig. 2b, where a sketch of the bottom of the e_g conduction bands for different gate biases, i.e., different perpendicular electric fields, is depicted. The e_g bands are assumed to be contacted by the source and drain electrodes, and govern the device transport. Upon the application of an electric field with the first pair of gate electrodes, the e_g bands split. If $V_{g1} > 0$ (meaning the electric field points from the top to the bottom of the stack) the first double-gate enables spin-up transport and blocks spin-down carriers, by populating the bottom CrI$_3$ layer and depleting the top one. If $V_{g1} < 0$ (meaning the electric field points from the bottom to the top of the stack), spin-down transport is enabled by populating the top CrI$_3$ layer and depleting the bottom one, thus acting as spin filter.

Within the underlapped spacer region, i.e., after the first couple of gates, we have thus only one type of spin carriers. When the

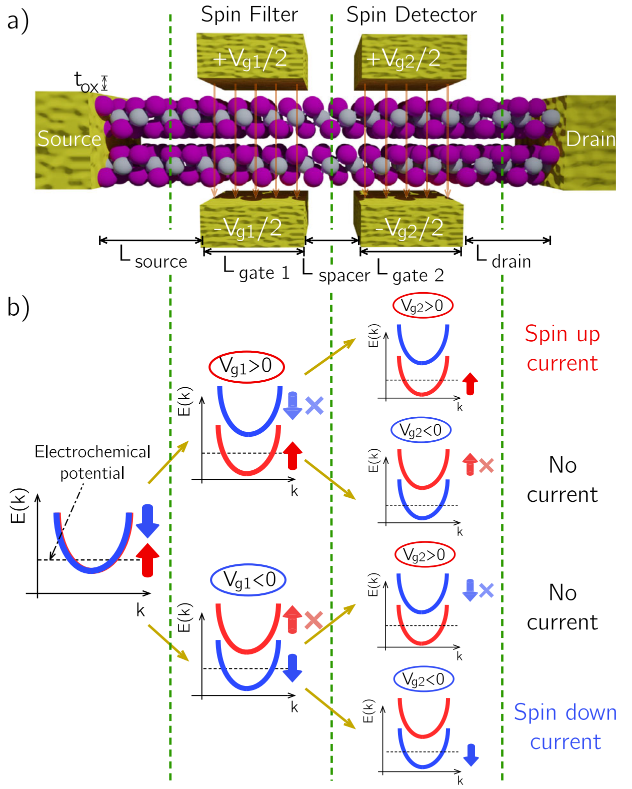

Fig. 2 Proof-of-concept spin logic device. **a** Schematic of the device architecture with the main geometrical parameters. **b** Pictorial sketch of the spin polarized e_g conduction band structure for the filtering and detecting mechanism in the case of net spin up current, net spin down current and no current for different values of V_{g1} and V_{g2}.

spin-polarized carriers enter into the channel region that is under the influence of the second double-gate configuration, two different scenarios arise: (i) if the same polarity as in V_{g1} is applied to V_{g2}, spin-up or spin-down carriers pass through the second double gate, resulting in a net spin current at the drain contact; (ii) if an opposite polarity is applied at V_{g2}, on the contrary, spin carriers are blocked, as depicted in Fig. 2b, and the current reaching the drain contact is negligible. Therefore, the second double gate actively works as a spin current detector. It is worth noting that the first and the second double-gate configurations are structurally identical. Their distinct operation and role in the overall device are a consequence of the spin nature of the injected current: while in the first double gate the incoming current is not spin-polarized, in the second double gate it is, resulting in the different filtering and detecting functionalities, respectively.

Thus, the overall device is able to provide, upon the application of proper biases V_{g1} and V_{g2}, spin-up and spin-down polarized currents or nearly zero current, enabling a complete platform for spin current processing controlled by a two double-gate configuration and exploiting an unique channel material.

Multiscale simulations of bilayer CrI$_3$-based device

In order to investigate the proposed device concept and evaluate its performance as a spin-valve transistor, we use a multiscale approach combining ab initio DFT calculations, maximally localized Wannier functions[39] and non-equilibrium transport calculations using the Green's functions approach[40]. The transmission through the device is solved self-consistently with the device electrostatics using the NanoTCAD ViDES[41,42] device simulation code (see the Methods for more details on the DFT, Wannier and transport calculations).

In order to get better insights on the main physical mechanisms at play in the proposed device, we have first investigated an isolated double-gate configuration, i.e., the first half of the device in Fig. 2a, since it constitutes the fundamental block of the spin processing

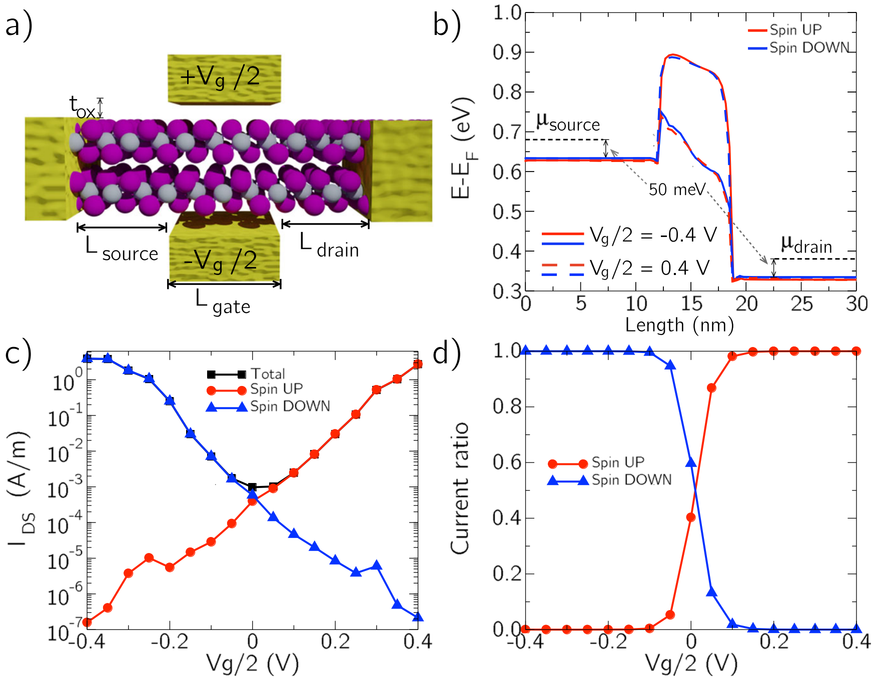

Fig. 3 Spin filter device. **a** Schematic depiction of the spin filter device with indicated the main geometrical parameters. **b** Conduction band for spin up and spin down for $V_g/2 = -0.4$ V (solid lines) and $V_g/2 = 0.4$ V (dashed lines). **c** Total current (black), spin up current (red) and spin down current (blue) as a function of $V_g/2$. **d** Current ratio as a function of $V_g/2$.

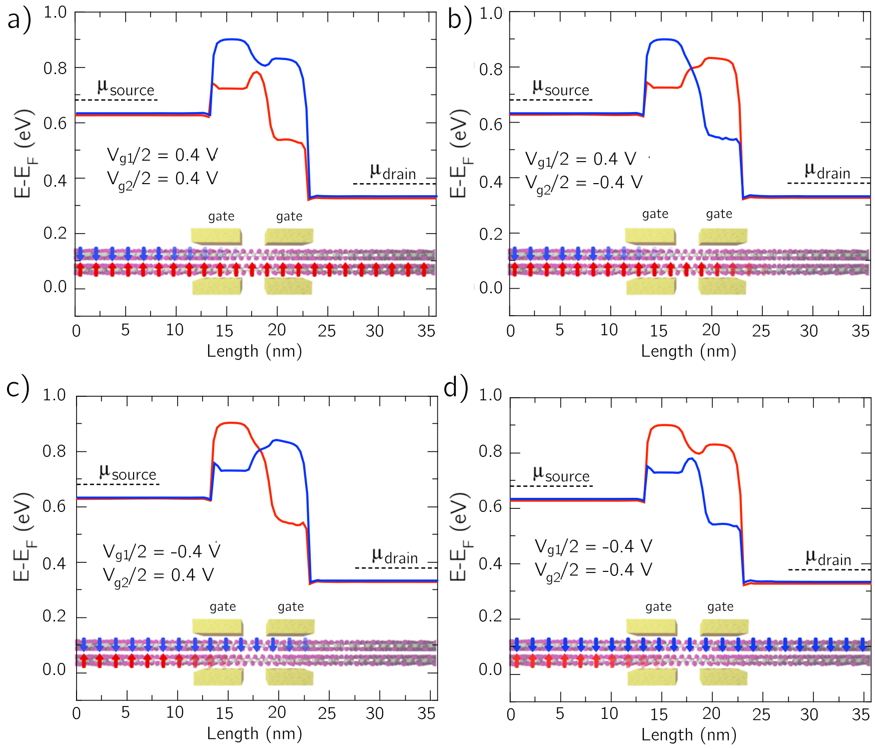

Fig. 4 Conduction band profile for the spin-valve transistor. Spin polarized conduction band profile for **a** $V_{g1}/2 = 0.4$ V and $V_{g2}/2 = 0.4$ V; **b** $V_{g1}/2 = 0.4$ V and $V_{g2}/2 = -0.4$ V; **c** $V_{g1}/2 = -0.4$ V and $V_{g2}/2 = 0.4$ V; **d** $V_{g1}/2$ = -0.4 V and $V_{g2}/2 = -0.4$ V. Fermi levels at the source and at the drain are indicated. At the bottom of each plot a schematic depiction of the device with spin carrier populations is reported.

platform. Figure 3a shows a schematic picture of the spin filter device with double-gate configuration and contacted by source and drain electrodes at both ends. In particular, in order to fix the difference between the electrochemical potential μ at the source and drain contacts with respect to the bottom of the conduction band, we have considered a fixed charge doping in these regions, resulting in a energy difference of 50 meV (see Fig. 3b). We have considered an applied bias V_{ds} of 0.3 V, $L_{source/drain} = 12$ nm, $L_{gate} =$ 6 nm and $t_{ox} = 0.5$ nm, with a dielectric constant of 3.9 both in the oxide and in the bilayer region. Transport simulations have been performed at 45 K, i.e., at the Curie temperature of bilayer CrI_3. Since the injected carriers from the source are not initially spin-polarized, the device is expected to effectively operate as a spin filter.

In Fig. 3b, we show the bottom of the conduction band for spin-up (red) and spin-down (blue) carriers along the device for two opposite V_g biases (i.e., opposite electric fields). First, we observe that the electric field produces a splitting of the spin-up and spin-down conduction bands, in agreement with the DFT results reported in the previous section, but now calculated in a self-consistent way, considering the device electrostatics. As a consequence, for $V_g < 0$ (solid lines), spin-down carriers see a lower channel barrier than spin-up carriers, resulting in a higher transmission for spin-down states than for spin-up ones. The opposite happens for $V_g > 0$ (dashed lines), namely spin-up carriers are transmitted from the source to the drain with high probability, while spin-down carriers are not. This is further confirmed by the spin polarized current shown in Fig. 3c, where it can be observed that for $V_g/2 = \pm 0.4$ V, the difference between the two spin-polarized currents is around 8 orders of magnitude. Finally, in Fig. 3d, we present the current ratio ($I_{up/down}/I_{tot}$), showing a spin current filtering higher than 99% already for $|V_g/2| > 0.25$ V. Two important aspects are worth to be highlighted: (i) the spin currents are as high as ~3 A/m, for a device length of 6 nm; (ii) the maximum electric field needed to spin filter the charge current is 0.28 V/nm between the CrI_3 layers, that is well below the critical value for the AFM to FM transition (~0.8 V/nm on SiO_2[19]) and is 0.88 V/nm in the oxides (below the breakdown field of SiO_2, i.e., ~1.0 V/nm).

Now we discuss the full proof-of-principle device presented in Fig. 2a. For this device, we consider source and drain regions of length $L_{source/drain} = 14$ nm, gate lengths $L_{gate_{1/2}} = 4$ nm and a spacer between both couple of gates of $L_{spacer} = 2$ nm. The total channel length is 10 nm and the equivalent oxide thickness $t_{ox} =$ 0.5 nm with a dielectric constant of $\epsilon = 3.9$. We assume the same amount of doping in the source and drain regions as before, while we do not assume any doping in the spacer region.

In Fig. 4, we report the conduction-band profiles along the device for four different bias configurations: (a) both V_{g1} and V_{g2} positive; (b) V_{g1} positive and V_{g2} negative; (c) V_{g1} negative and V_{g2} positive; (d) both V_{g1} and V_{g2} negative. At the bottom of each plot we show a schematic picture of the device along with the spin carrier populations in each layer. When V_{g1} and V_{g2} have the same polarity spin-up (a) or spin-down (d) carriers see a low barrier in both gate regions. As a consequence a net current of spin-up (a) or spin-down (d) is transmitted from the source and to the drain. On the contrary, when V_{g1} and V_{g2} have opposite polarity (b and c), the second double-gate creates a high energy barrier for the spin flavor filtered in gate 1. Thus, the second couple of gates prevents the spin-up (b) or spin down (c) carriers to reach the drain and a negligible net current is collected.

In Fig. 5a, b, we report the spin-up, spin-down, and total currents as a function of V_{g2} for two fixed values of V_{g1}, i.e., $V_{g1}/2 = -0.4$ V in (a) and $V_{g1}/2 = 0.4$ V in (b), respectively. It can be observed that, when the two gates are polarized in the same way, the spin-polarized current is in the range of 10^{-4}–10^{-3} A/m, while when the two gates present an opposite electric field polarization, the spin-polarized current is roughly 2 order of magnitude smaller (10^{-6} A/m). As expected, the increasing channel length and the spacer region without gate lower the tunneling current compared to the spin filter device; however, it is still within the range of detection of the actual current probes. The dependence of the spin-polarized and total

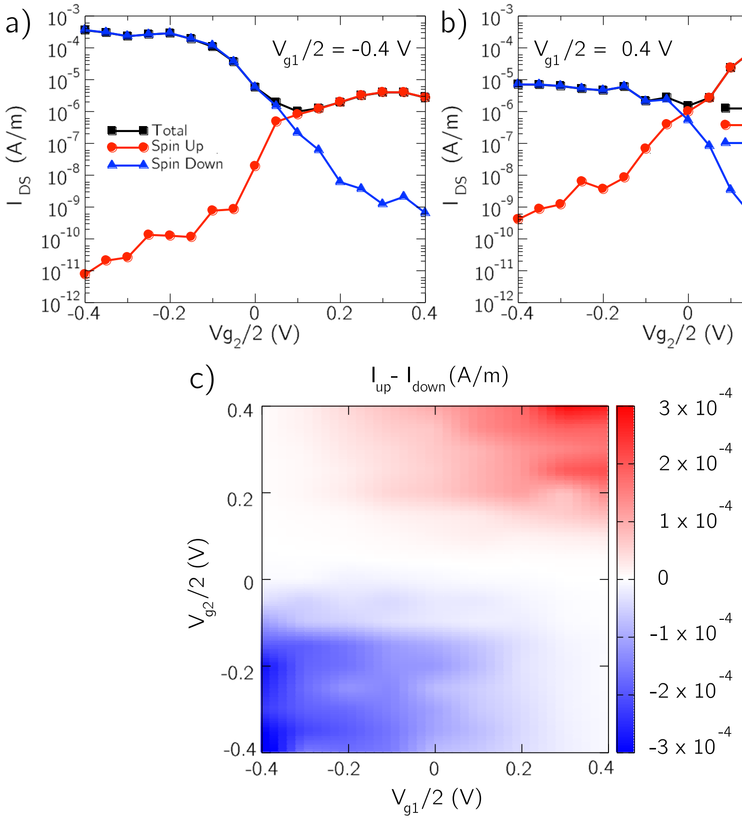

Fig. 5 Spin polarized current for the spin-valve transistor. Total, spin-up, and spin-down currents as a function of V_{g2} for **a** $V_{g1}/2 = -0.4$ V and **b** $V_{g1}/2 = 0.4$ V. **c** Color map of the difference between spin-up current (I_{up}) and spin-down current (I_{down}) as a function of V_{g1} and V_{g2}.

currents on the different gate and spacer lengths is reported in the Supplementary Information. We also remark that a potential improvement in the Curie temperature would imply a higher thermionic injection and thus an increased source-to-drain current.

Finally, in Fig. 5c we present a color map of the difference between the spin-up (I_{up}) and the spin-down (I_{down}) currents as function of both V_{g1} and V_{g2}. We can clearly identify three different regions, the top right corner (red color), i.e., both V_{g1} and V_{g2} positive, where spin-up current is predominant, the bottom left corner (blue color), i.e., both V_{g1} and V_{g2} negative, where spin-down current is preponderant and the remaining two quadrants, i.e., with opposite V_{g1} and V_{g2}, which show almost no current compared to the other two quadrants.

We have proposed a lateral spin-valve transistor concept based on bilayer CrI_3 using a split double-gate configuration that can be used as a unified platform for spintronic applications. This fully electrically controlled lateral spin device is able to both filter and detect spin carriers by tuning the electrical and spin properties of bilayer CrI_3 with an external electric field. In order to have detectable spin-polarized currents, the device operates in the ballistic regime, which is a reasonable assumption given the nanometer-sized dimensions of the channel. The electric field required for full operation is half of the reported critical value for the interlayer magnetic switching in bilayer CrI_3, and reduces the need of a constant magnetic bias. The proposed spin device has the potential of yielding spin polarization (up to 99%) and ON/OFF current ratio (~10^2), which makes it a promising candidate for future spintronic applications. Finally, we have demonstrated that, by properly tuning the two gate regions, it is possible to select between *up*, *down*, and *zero* spin polarized current, opening unexplored routes towards the design of spin logic devices based on 2D nano-magnets. It is worth stressing that the device concept presented here can be extended and realized in other emerging 2D nano-magnets such as the recently discovered $CrPS_4$, the high-T_C CrSBr and CrSeBr ferromagnetic semiconductors, and also the recently synthesized ultrathin Co-based ferrite nanosheets.

METHODS

Density functional theory calculations

Density Functional Theory calculations have been performed with the Quantum Espresso suite[38]. We use projector augmented-wave pseudopotentials (PAW) within the Perdew–Burke–Ernzerhof (PBE) approximation for the exchange-correlation functional. The bilayer CrI_3 geometry has been relaxed until all forces are smaller than 0.051 eV/Å. Grimme-D2 correction is used to include van der Waals forces during relaxation. For the electronic structure calculations, we use an energy convergence threshold of 10^{-6} Ry, and a $4 \times 4 \times 1$ k-mesh grid. The calculations are carried out in absence of spin-dependent interactions.

Wannier calculations

Wannierization procedure has been performed with Wannier90 code[39] on a $4 \times 4 \times 1$ k-mesh grid projecting only on the $\{d_{x^2-y^2}, d_{z^2}\}$ orbitals of the Cr atoms with spin up for the bottom layer and spin down for the top layer.

Transport calculations

Transport calculations have been performed using NanoTCAD ViDES[41,42] simulator which solves self-consistently the non-equilibrium Green's functions with the Poisson equation in the ballistic regime. We have considered a spacing in energy of 10^{-4} eV and 60 k-modes in the direction perpendicular to transport. The electrostatic is solved fixing Dirichlet conditions on the top/bottom gates, while Neumann conditions are considered elsewhere on the boundaries. Convergence on the potential has been assured when the difference between two iterations is smaller than 8×10^{-3} in each point of the grid.

DATA AVAILABILITY

The data that support the findings of this study are available from the authors upon request.

Received: 5 August 2022; Accepted: 18 May 2023;
Published online: 26 June 2023

REFERENCES

1. Gong, C. et al. Discovery of intrinsic ferromagnetism in two-dimensional van der Waals crystals. *Nature* **546**, 265–269 (2017).
2. Huang, B. et al. Layer-dependent ferromagnetism in a van der Waals crystal down to the monolayer limit. *Nature* **546**, 270–273 (2017).
3. Gibertini, M., Koperski, M., Morpurgo, A. F. & Novoselov, K. S. Magnetic 2D materials and heterostructures. *Nat. Nanotechnol.* **14**, 408–419 (2019).
4. Soriano, D., Katsnelson, M. I. & Fernández-Rossier, J. Magnetic two-dimensional chromium trihalides: a theoretical perspective. *Nano Lett.* **20**, 6225–6234 (2019).
5. Cardoso, C., Soriano, D., García-Martínez, N. A. & Fernández-Rossier, J. Van der Waals spin valves. *Phys. Rev. Lett.* **121**, 067701 (2018).
6. Karpiak, B. et al. Magnetic proximity in a van der Waals heterostructure of magnetic insulator and graphene. *2D Mater.* **7**, 015026 (2019).
7. Ghiasi, T. S. et al. Electrical and thermal generation of spin currents by magnetic bilayer graphene. *Nat. Nanotechnol.* **16**, 788 (2021).
8. Zhong, D. et al. Van der Waals engineering of ferromagnetic semiconductor heterostructures for spin and valleytronics. *Sci. Adv.* **3**, e1603113 (2017).
9. Seyler, K. L. et al. Valley manipulation by optically tuning the magnetic proximity effect in wse2/cri3 heterostructures. *Nano Lett.* **18**, 3823–3828 (2018).
10. Zhong, D. et al. Layer-resolved magnetic proximity effect in van der Waals heterostructures. *Nat. Nanotechnol.* **15**, 187–191 (2020).
11. Lyons, T. P. et al. Interplay between spin proximity effect and charge-dependent exciton dynamics in $MoSe_2/CrBr_3$ van der Waals heterostructures. *Nat. Commun.* **11**, 6021 (2020).
12. Soriano, D. & Lado, J. L. Exchange-bias controlled correlations in magnetically encapsulated twisted van der Waals dichalcogenides. *J. Phys. D Appl. Phys.* **53**, 474001 (2020).
13. Kezilebieke, S. et al. Topological superconductivity in a van der Waals heterostructure. *Nature* **588**, 424 (2020).
14. Sivadas, N., Okamoto, S., Xu, X., Fennie, CraigJ. & Xiao, D. Stacking-dependent magnetism in bilayer cri_3. *Nano Lett.* **18**, 7658–7664 (2018).
15. Soriano, D., Cardoso, C. & Fernandez-Rossier, J. Interplay between interlayer exchange and stacking in cri_3 bilayers. *Solid State Commun.* **299**, 113662 (2019).
16. Klein, D. R. et al. Probing magnetism in 2D van der Waals crystalline insulators via electron tunneling. *Science* **360**, 1218–1222 (2018).
17. Wang, Z. et al. Very large tunneling magnetoresistance in layered magnetic semiconductor cri_3. *Nat. Commun.* **9**, 2516 (2018).
18. Song, T. et al. Giant tunneling magnetoresistance in spin-filter van der Waals heterostructures. *Science* **360**, 1214–1218 (2018).
19. Jiang, S., Shan, J. & Mak, KinFai Electric-field switching of two-dimensional van der Waals magnets. *Nat. Mater.* **17**, 406–410 (2018).
20. Huang, B. et al. Electrical control of 2D magnetism in bilayer CrI_3. *Nat. Nanotechnol.* **13**, 544–548 (2018).
21. Jiang, S., Li, L., Wang, Z., Mak, K. F. & Shan, J. Controlling magnetism in 2D CrI_3 by electrostatic doping. *Nat. Nanotechnol.* **13**, 549–553 (2018).
22. Jiang, S., Li, L., Wang, Z., Shan, J. & Mak, K. F. Spin tunnel field-effect transistors based on two-dimensional van der Waals heterostructures. *Nat. Electron.* **2**, 159–163 (2019).
23. Soriano, D. & Katsnelson, M. I. Magnetic polaron and antiferromagnetic-ferromagnetic transition in doped bilayer CrI_3. *Phys. Rev. B* **101**, 041402 (2020).
24. Ohno, H. et al. Electric-field control of ferromagnetism. *Nature* **408**, 944–946 (2000).
25. Liu, T. et al. Spin caloritronics in a $crbr_3$-based magnetic van der Waals heterostructure. *Phys. Rev. B* **101**, 205407 (2020).
26. Ghiasi, T. S. et al. Electrical and thermal generation of spin currents by magnetic bilayer graphene. *Nat. Nanotechnol.* **16**, 788–794 (2021).
27. Zhao, B. et al. Room temperature spin-valve with van der Waals ferromagnet Fe_5GeTe_2/graphene heterostructure. *Adv. Mater.* **35**, e2209113 (2023).
28. Marin, E. G., Marian, D., Iannaccone, G. & Fiori, G. Tunnel-field-effect spin filter from two-dimensional antiferromagnetic stanene. *Phys. Rev. Appl.* **10**, 044063 (2018).
29. Marin, E. G., Marian, D., Iannaccone, G. & Fiori, G. First principles investigation of tunnel fets based on nanoribbons from topological two-dimensional materials. *Nanoscale* **9**, 19390–19397 (2017).
30. Peng, Y. et al. Magnetic structure and metamagnetic transitions in the van der Waals antiferromagnet crps4. *Adv. Mater.* **32**, 2001200 (2020).
31. Telford, E. J. et al. Layered antiferromagnetism induces large negative magnetoresistance in the van der Waals semiconductor crsbr. *Adv. Mater.* **32**, 2003240 (2020).
32. Wu, F. et al. Quasi-1D electronic transport in a 2d magnetic semiconductor. *Adv. Mater.* **34**, 2109759 (2022).
33. Klein, J. et al. Control of structure and spin texture in the van der Waals layered magnet crsbr. *Nat. Commun.* **13**, 5420 (2022).
34. Wang, H., Qi, J. & Qian, X. Electrically tunable high curie temperature two-dimensional ferromagnetism in van der Waals layered crystals. *Appl. Phys. Lett.* **117**, 083102 (2020).
35. Cheng, R. et al. Ultrathin ferrite nanosheets for room-temperature two-dimensional magnetic semiconductors. *Nat. Commun.* **13**, 5241 (2022).
36. Thiel, L. et al. Probing magnetism in 2D materials at the nanoscale with single-spin microscopy. *Science* **364**, 973–976 (2019).
37. Meseguer-Sánchez, J. et al. Layer-dependent ferromagnetism in a van der Waals crystal down to the monolayer limit. *Nat. Commun.* **21**, 6265 (2021).
38. Giannozzi, P. et al. Quantum espresso: a modular and open-source software project for quantum simulations of materials. *J. Phys. Condens. Matter* **21**, 395502 (2009).
39. Mostofi, A. A. et al. wannier90: A tool for obtaining maximally-localised Wannier functions. *Comp. Phys. Commun.* **178**, 685–699 (2008).
40. Datta, S. Nanoscale device modeling: the Green's function method. *Superlattices Microstruct.* **28**, 253–278 (2000).
41. NanoTCAD ViDES. http://vides.nanotcad.com/vides/ (2023).
42. Marian, D., Marin, E. G., Perucchini, M., Iannaccone, G. & Fiori, G. Multi-scale simulations of two dimensional material based devices: the NanoTCAD ViDES suite. *J. Comput. Electron.* https://doi.org/10.1007/s10825-023-02048-2 (2023).

ACKNOWLEDGEMENTS

The authors gratefully acknowledge Graphene Flagship Core 3 (Contract No. 881603). Work partially supported by the Italian Ministry of Education and Research (MIUR) in the framework of the FoReLab project (Departments of Excellence). The authors thank Efren Navarro-Moratalla for useful discussions.

AUTHOR CONTRIBUTIONS

D.S. and D.M. carried out first-principles calculations. D.M., E.C., and E.G.M. performed spin-transport simulations. G.F., D.S., D.M., and E.G.M. conceived the project. G.F. supervised the work. All authors contributed to the discussion and manuscript writing.

COMPETING INTERESTS

The authors declare no competing financial or non-financial interests. Author Gianluca Fiori is a member of the Editorial team for *npj 2D Materials and Applications* and, as such, was not involved in the journal's review of, or decisions related to, this manuscript.

ADDITIONAL INFORMATION

Supplementary information The online version contains supplementary material available at https://doi.org/10.1038/s41699-023-00400-5.

Correspondence and requests for materials should be addressed to Damiano Marian or Gianluca Fiori.

Reprints and permission information is available at http://www.nature.com/reprints

Publisher's note Springer Nature remains neutral with regard to jurisdictional claims in published maps and institutional affiliations.

Open Access This article is licensed under a Creative Commons Attribution 4.0 International License, which permits use, sharing, adaptation, distribution and reproduction in any medium or format, as long as you give appropriate credit to the original author(s) and the source, provide a link to the Creative Commons license, and indicate if changes were made. The images or other third party material in this article are included in the article's Creative Commons license, unless indicated otherwise in a credit line to the material. If material is not included in the article's Creative Commons license and your intended use is not permitted by statutory regulation or exceeds the permitted use, you will need to obtain permission directly from the copyright holder. To view a copy of this license, visit http://creativecommons.org/licenses/by/4.0/.

© The Author(s) 2023